RESEARCH ARTICLE
doi: 10.2306/scienceasia1513-1874.2026.068

ScienceAsia 52 (4): 2026: ID 2026068: **1–8**

Preparation of high-surface-energy nickel surface by electrodeposition combined with chemical etching

Bowen Yue[a,*], **Lijiang Shao**[b]

[a] School of Automobiles and Low-Altitude Unamnned Aerial Vehides, Zibo Polytechnic University, Zibo 255300 China
[b] College of Information Engineering, Wenzhou Business College, Wenzhou 325035 China

[*]Corresponding author, e-mail: yuebowen@foxmail.com

Received 22 Jan 2026, Accepted 2 Jul 2026
Available online 19 Jul 2026

ABSTRACT: Amorphous soft magnetic strips require highly hydrophilic copper cooling rolls to guarantee rapid heat transfer and uniform solidification. In this work, hydrophilic nickel coatings were prepared on copper substrates using electrodeposition combined with $FeCl_3$ etching. The influences of four key parameters, including the molar ratio of anions in the solution, brightener, etching concentration, and current density, were studied via response surface methodology and uncertainty analysis. Results show that the optimized sample exhibits a surface free energy of 55.20 mJ/m^2, which is 4.07% higher than that of the control group, and its polar component reaches 7.99 mJ/m^2, 14.8% higher than those of the other groups. Brightener and etching solution concentrations have the most significant impact on wettability variation, with the maximum interquartile ranges reaching 0.95 and 1.78, respectively, while the effects of deposition ratio and current density are relatively weak. Rough etched surfaces favor the formation of NiO and $Ni(OH)_2$ polar phases. Together with the Wenzel wetting mechanism, the high surface energy and micro-roughness work synergistically to improve surface hydrophilicity. This work provides a practical approach for designing highly hydrophilic nickel-modified cooling rolls for high-quality amorphous strip manufacturing.

KEYWORDS: nickel coatings, uncertainty analysis, surface wettability, surface free energy, electrochemical deposition

INTRODUCTION

As a soft magnetic material, amorphous strips exhibit high saturation magnetization, high permeability, and low coercivity, making them well-suited for high-precision, high-stability, and highly integrated electronic applications [1, 2]. These strips are typically produced by the planar flow casting method, in which molten alloy impinges onto a rotating copper cooling roll, spreads under adhesion, and rapidly solidifies into an amorphous structure before being ejected by centrifugal force [3, 4]. The wettability of the cooling roll surface plays a critical role in determining the spreading behavior of the molten metal [5]. A hydrophilic surface can enhance the solid–liquid contact area, accelerate heat transfer during phase change, and increase the solidification rate [6], thereby facilitating the production of thin amorphous strips with uniform composition and superior properties [7]. At present, polished copper is widely employed as the cooling roll surface. Nevertheless, it is susceptible to wear and fatigue cracking when operating at temperatures near 573 K [8], which results in localized damage and inconsistent wettability. These defects frequently induce fluctuations in strip width and the formation of crystalline phases on the air-facing side of the strips [9].

Nickel and nickel-based alloys exhibit excellent strength, hardness, and wear resistance at elevated temperatures and have been widely employed in hot-forming rollers to prolong service life [10]. Given the similarity between the operating environment of copper cooling rolls and that of casting rollers [11], recent studies have focused on preparing hydrophilic layers with tailored microstructures [12]. Xu et al [13] fabricated stable Ni-SiC coatings via magnetic field-assisted scanning electrodeposition. The as-prepared coatings showed strong hydrophilicity, with water droplets fully wetting the surface within 2 s. Li et al [14] used the micro-arc oxidation method to adjust the power supply voltage and current to create a rough surface morphology, thereby obtaining an ultra-hydrophilic surface with a contact angle close to 0°. Surface modification carried out by chemical etching has been proven to enhance hydrophilicity and surface energy more effectively than traditional method [15]. However, the influence of key process parameters on the nickel layer has not been deeply studied. Therefore, more in-depth research should be conducted to explore the coupling laws among these factors.

In this study, we combined electrodeposition and surface etching to fabricate nickel surfaces. An uncertainty analysis approach was employed to evaluate the coupling effects of key process parameters on surface free energy and wetting behavior. Surface morphology and roughness were characterized to elucidate the mechanism underlying the high surface energy state. This approach provides a rapid and effective method for preparing highly hydrophilic surfaces, providing both theoretical insight and practical guidance for the design of high-performance amorphous strip production systems.

MATERIALS AND METHODS

The anode was fabricated from a 99.9 wt% nickel sheet, which was cut into dimensions of 50 mm × 30 mm × 2 mm. A 99.9 wt% copper block, machined to 25 mm × 25 mm × 2 mm, served as the cathode substrate. All plates were progressively ground using silicon carbide paper up to a 2,500 grit size. Prior to deposition, the substrates underwent a multistep cleaning procedure: they were first ultrasonically cleaned in an alkaline solution containing 0.3 mol/l Na_2CO_3, 0.15 mol/l Na_3PO_4, and 1.5 ml/l OP-10 at 353 K for 15 min, followed by sequential ultrasonic rinsing in distilled water and ethanol for 15 min each. Subsequently, electrochemical polishing was conducted in 14.7 mol/l H_3PO_4 at a current density of 6 A/dm^2 for 10 min. The samples were then rinsed with acetone and distilled water and transferred into the electrodeposition bath [16]. Fig. 1 shows a schematic diagram of the combined electrodeposition and etching process. The electrodeposition bath used $NiSO_4$ and $NiCl_2$ as the nickel ion sources, with the total Ni^{2+} concentration fixed at 1.2 mol/l. The molar ratio of $NiSO_4$ to $NiCl_2$ was changed from 1 to 5. The bath also included 0.4 mmol/l SDS as a wetting agent and H_3BO_3 as a pH buffer, maintaining the solution pH at 3.5. Sodium saccharin ($C_7H_4NO_3SNa$) acted as a brightener, with concentration ranging from 0 to 2 mmol/l. The bath temperature was maintained at 348 K, and the solution was stirred continuously at 600 rpm. The anode-cathode distance was set to 15 mm. Deposition was carried out under direct current conditions, with current densities varying between 2–8 A/dm^2. After deposition, the samples were rinsed with deionized water, air-dried, and subjected to subsequent etching treatment. The etching treatment was performed using a solution composed of 0.6 to 1.8 mol/l $FeCl_3$, 0.4 mol/l H_2O_2, and 0.15 mol/l HCl [15]. The as-deposited nickel coatings were immersed in mixed solution for 5 min under ambient conditions. Following etching, the samples were ultrasonically cleaned in ethanol for 10 min and subsequently dried in an oven at 338 K for 20 min. All chemical reagents used in this work were obtained from Aladdin Chemistry Co., Ltd., Shanghai, China.

To evaluate the factors influencing the sample surface wettability, four key independent variables were selected: $NiSO_4 \cdot 6H_2O$ and $NiCl_2 \cdot 6H_2O$ (K), the concentration of brightener in the bath (c_b), the ferric chloride concentration of etching solution (c_e), and the cathode current density (J). Thirty groups of experiments with four variables were established by the CCD method (Table S1) [17]. The static contact angles on the sample surfaces were measured at 293 K with an optical contact angle analyzer (OCA-25; Data Physics Instruments GmbH, Germany). A 5 µl volume of probe liquid was dropped onto the surface. For each liquid, measurements were taken at five distinct locations on the same sample, with three repeated measurements per location. The standard deviation was required to be less than 1°; otherwise, the measurement was repeated. The final reported value represents the average of all valid measurements. The surface morphology of the etched nickel layers was examined using a scanning electron microscope (SEM, QUANTA FEG 250, FEI, USA) at a magnification of 30,000× under high vacuum conditions. Additionally, a 3D digital microscope (DSX10-TF, Olympus Corporation, Japan) operating at 7000 × magnification was employed to quantify the surface roughness across multiple regions of each specimen.

RESULTS AND DISCUSSION

Surface feature

The reaction between the nickel layer and the etching solution is shown in Eqs. (1)–(3).

$$Ni + 2Fe^{3+} \rightarrow Ni^{2+} + 2Fe^{2+} \quad (1)$$

$$Ni + 2H^{+} \rightarrow Ni^{2+} + 2H_2\uparrow \quad (2)$$

$$Ni + 2Fe^{3+} \rightarrow Ni^{2+} + 2Fe^{2+} \quad (3)$$

Fig. 2 presents SEM images of the etched nickel coatings prepared under different processing conditions. Sample 1, fabricated with intermediate parameter levels, was used as the control group (Fig. 2a). It has many scale-like protrusions, with lengths ranging from 0.5 to 1 µm. Fig. 2b corresponds to a coating deposited from a solution with high chloride ion concentration ($K = 1$). After etching, a fault rock-like structure with clearly sharp ridges can be seen. In contrast, the sample prepared with high sulfate concentration ($K = 5$, Fig. 2c) has a relatively smooth surface, composed of small stone-like features about 200 nm or smaller. When no brightener was used (Fig. 2d), the coating had a rough morphology after etching, with large cavities up to 6 µm in diameter. Each cavity contains clear, uniformly stacked block structures. On the other hand, the sample prepared with a high brightener content (Fig. 2e) remained smooth after etching, covered with evenly dispersed micro-convex structures about 100 nm in size. After treatment with a low-concentration $FeCl_3$ solution ($c_e = 0.6$ mol/l, Fig. 2f), the larger surface protrusions were dissolved, while the underlying hierarchical microstructure remained intact. As $FeCl_3$ concentration increased ($c_e = 1.8$ mol/l, Fig. 2g), the corrosion effect became stronger. This reduced the height of the protrusions and formed uniformly arranged nanopores about 200 nm in diameter.

To quantify the morphological variations among the samples, surface characterization was performed using a 3D digital microscope (Fig. 3), and surface roughness was obtained (Table S2). The arithmetic average roughness (R_a) reflects the absolute mean deviation of the profile peaks and valleys from the

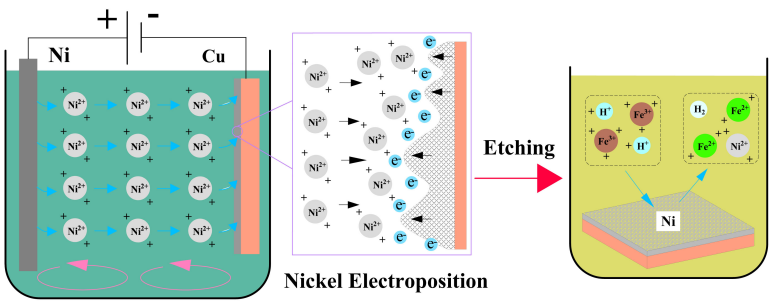

Fig. 1 The schematic diagram for fabricating the surface morphology.

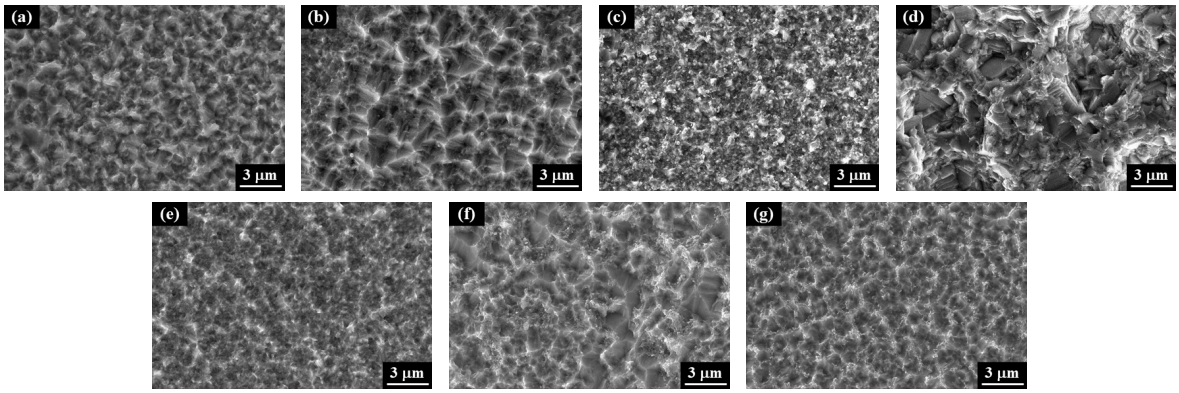

Fig. 2 Surface morphologies with different samples: (a–g) Samples 1–7.

central line, while the root mean square roughness (R_q) indicates the standard deviation of surface height distribution. The control group exhibited an R_a value of 321 nm. In contrast, Sample 5 showed the lowest roughness among all etched nickel layers, with an R_a of 222 nm. Samples 2 and 4 displayed higher roughness values, measuring 452 nm and 508 nm, respectively. These results show that a lower concentration of brightening agents during deposition helps form rougher surface features. Similarly, a higher chloride ion concentration in the plating solution was also linked to increased surface roughness [18]. Furthermore, the ratio of anions in the electrolyte has a significant impact on the final surface morphology [19]. For instance, increasing the nickel sulfate concentration within an appropriate range has been reported to produce coatings with lower roughness.

Surface contact angle

The water contact angles of the prepared surfaces are shown in Table S1. In order to study the coupled influence of four variables on the water contact angle (CA), the response surface methodology was selected

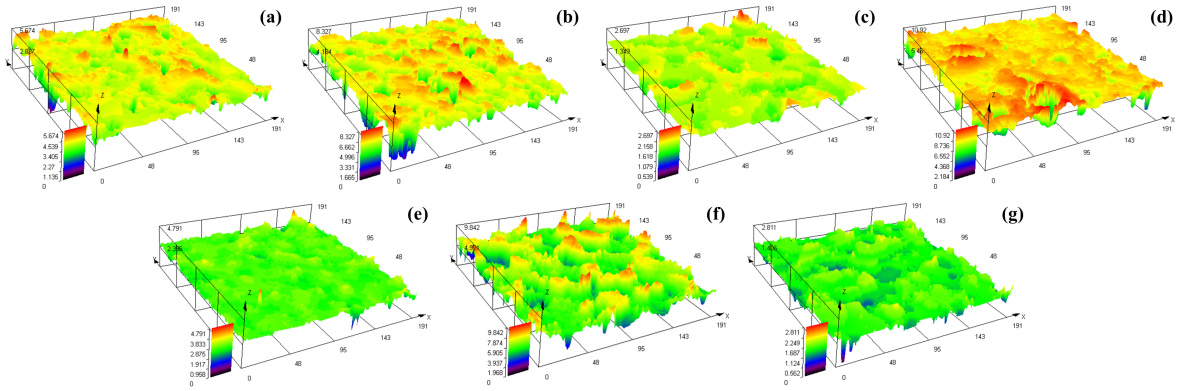

Fig. 3 3D surface feature images of the samples: (a–g) Samples 1–7.

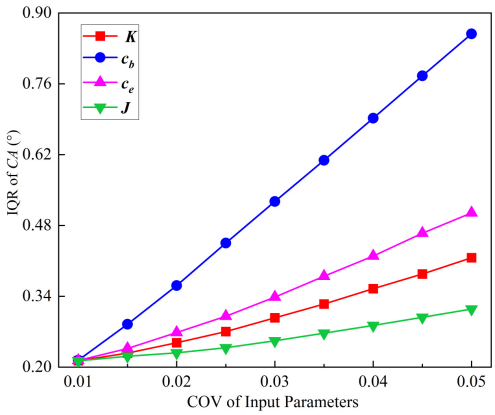

Fig. 4 IQR of CA at different COVs of the input parameters.

to establish relationships as follows [20].

$$\mathrm{CA} = 15.23 + 4.40K + 13.29c_b - 20.28c_e - 0.46J + 0.36Kc_b + 0.91c_bJ - 0.19K^2 - 1.23c_b^2 + 8.96c_e^2 \quad (4)$$

An uncertainty analysis was performed to evaluate the effects of key parameters on the wettability of the coating surface [21–23]. The mean values of all variables were assumed to be as follows: $K = 3$, $c_b = 1$ mmol/l, $c_e = 1.2$ mol/l, $J = 5$ A/dm^2, and set the coefficient of variance (COV) for each input variable to 0.01 [24]. Latin hypercube sampling was employed to establish the sample set, which was sufficiently representative when the sample size exceeded 1,000 [25]. Owing to the large sample size and mutually independent nature of the measurements, and in accordance with previous studies [26], each variable can be reasonably assumed to obey a Gaussian distribution. The COV was used to describe the dispersion of variables. [27]. The COV of one variable varied between 0.01 and 0.05, while the other three variables remained at 0.01 [12]. Also, the value of the selected parameter varied randomly in the interval. The interquartile range (IQR) [28], defined as the difference between the 75th percentile and the 25th percentile, can be used to indicate the degree of dispersion of output parameters affected by an uncertainty variable. The final IQR values for all cases were calculated and plotted as shown in Fig. 4. Results show that the variability of the output is most significantly affected by the COV of c_b, followed by that of c_e, whereas the variations in J and K exert relatively weak influences.

Fig. 5 illustrates the IQR with different COVs of uncertain input parameters. When K ranges from 1 to 3, it has a weaker effect on water CA (Fig. 5a). However, if K exceeds 3, the IQR value increases significantly with increased COV, indicating a strong relationship between nickel sulfate concentration and contact angle. The maximum value of IQR is 0.393. When c_b exceeded 0.5, the IQR value increased significantly with increasing COV (Fig. 5b). This proves that brightener concentration has a significant impact on the CA of polar liquid. The IQR reached a peak of 0.95. Related studies have found that adjusting brightener concentration causes significant changes in surface morphology [29]. Moreover, after etching based on different surface characteristics, the obtained surface morphology and roughness still show significant differences. This indicates that the amount of the brightener is a key factor affecting the surface energy. Fig. S1 shows the trend of water CA with each variable under the RSM prediction. It can be found that the CA has been increasing rapidly with increasing brightener concentration, and the variation range was much larger than that of K. The IQR value was below 0.5 when c_e varied from 0.6 to 1.2 (Fig. 5c). When c_e reached 1.4, the IQR increased rapidly to 1.78. This shows that lower etching solution concentration has less effect on the surface water CA, but it is also higher than that of K. However, the CA value is sensitive to high concentration of etching solution. This is due to the fact that as c_e increases, water CA shows a tendency to decrease and then increase, with a minimum at c_e of 1.2. Subsequently, water CA has the fastest rate of increase compared to the other variables (Fig. 4). The IQR values show a smooth increasing trend (Fig. 5d). The increase in current density during deposition causes a more drastic degree of change in CA values [30]. However, it is not as important as the concentration of the etching solution and brightener. As the current density increases, the growth rate of water CA remains almost constant, and its value stabilizes between 30° and 40°.

The Wenzel model was used to analyze the relationship between surface roughness and wettability [30]. Eq. (5) describes the relationship among the intrinsic contact angle on an ideal smooth surface (θ_e), the roughness factor (r), and the apparent contact angle on the rough surface (θ_w).

$$\cos\theta_w = r \cdot \cos\theta_e \quad (5)$$

According to the Wenzel model, the liquid penetrates completely into the surface microstructures without entrapping air pockets, leading to a significant enlargement of the actual solid–liquid contact area as surface roughness increases. For an intrinsically hydrophilic material, a higher roughness factor enhances the solid–liquid interaction and reduces the energy barrier for wetting, thereby further decreasing the apparent contact angle and improving hydrophilicity.

Surface free energy and surface chemistry

The Van Oss-Chaudhury-Good method was applied to gauge the surface free energy (SFE) of etched coatings. The surface energy of solid (γ_s) and liquid (γ_l) consists of Lifshitz-Van der Waals interactions (γ^{LW}, the apolar component) and Lewis acid-base interactions (γ^{AB}, the polar component) [31, 32]. At least three

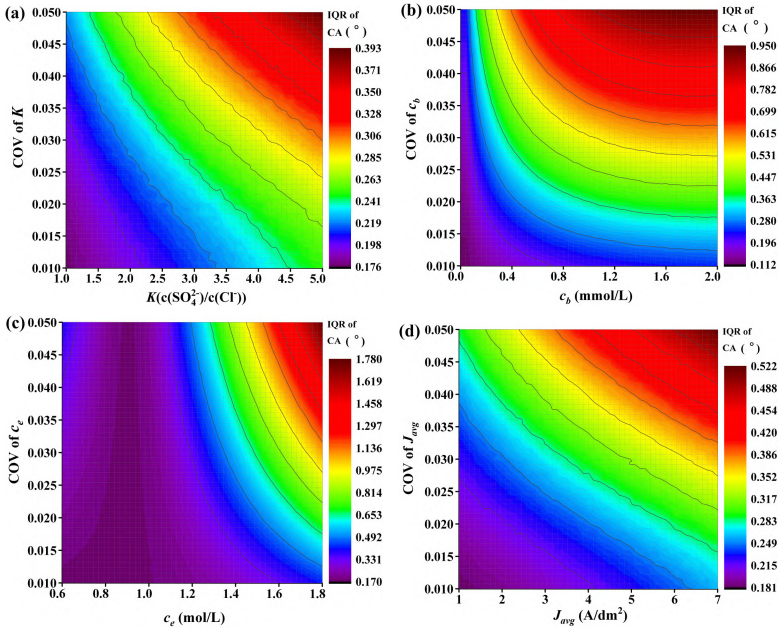

Fig. 5 IQR of CA at different COVs of uncertain input parameters: (a) K; (b) c_b; (c) c_e; (d) J_{avg}.

different probe liquids need to be selected to measure the contact angles of the solid, to obtain the unknown component of solid surface energy. Therefore, water (a polar liquid), glycerol (another polar liquid), and diiodomethane (an apolar liquid) were used as probe liquids in this study. The SFE of selected liquids was shown in Table S3 [33, 34].

The SFE of the different surfaces and their components were obtained by calculating as shown in Table S4, based on the contact angles that have been measured for the three liquids (Table S1). By comparison, it was found that γ_s and γ_s^{AB} varied significantly (10% and 25%, respectively) with deposition and etching parameters, but γ_s^{LW} changed little. Among all the experiments, the SFE and Lewis acid-base component of sample 4 were the highest, reaching 55.20 mJ/m^2 and 7.99 mJ/m^2, respectively, which were 4.07% and 14.8% higher than those of the control group. The lowest values for Sample 5 were 50.44 mJ/m^2 and 5.85 mJ/m^2, which were respectively 5.15% and 15.9% lower than those of the control group. It is seen that the variability in surface morphology and roughness induces a significant increase or decrease in the surface energy, especially the polar component [35]. Response surface methodology was also applied to study the coupled influence of four variables on the SFE of etched surface, as shown in Eqs. (6)–(7).

$$\gamma_s = 54.43 + 0.47K + 1.64c_b + 4.73c_e - 0.093J - 0.16Kc_b - 0.16c_bJ - 2.08c_e^2 \quad (6)$$

$$\gamma_s^{\text{AB}} = 8.51 - 0.45K - 0.71c_b + 1.53c_e - 0.038J - 0.076Kc_b - 0.082c_bJ + 0.039K^2 - 0.66c_e^2 + 0.0093J^2 \quad (7)$$

Similarly, uncertainty analysis was also used to measure significant changes in the factors affecting surface energy and Lewis acid-base component. Fig. 6 shows the IQRs of SFE with different COVs and input parameters. In terms of IQR for γ_s, the variability was affected significantly by the increasing variation of c_e, revealing a strong relationship between the etching and surface energy. In particular, when c_e is greater than 1.4, the IQR value rises rapidly, with a maximum value of 0.322, far higher than those of other input parameters. The curves show that γ_s has similar sensitivities to changes in K and c_b. The IQR change rate speeds up as K and c_b increase, with their peaks reaching 0.205 and 0.104, respectively. Therefore, brightener concentration has a more obvious effect on surface energy than chloride ion concentration. However, it is relatively unaffected by the variation with the COV of J. The maximum value of IQR is only 0.044. This indicates that the deposition current density has a weak effect on the surface energy of the etched samples. This suggests that the changes caused by current density during deposition converge to a consistent surface energy after etching. This is similar to the analysis of the contact angle.

The effect of the four process parameters on the Lewis acid-base component was shown in Fig. 7. It can be observed that the trend of IQR change was similar to that of SFE. The factor with the greatest impact on γ_s^{AB} was still c_e. When c_e exceeds 1.2 and continues to increase, the IQR value significantly increases with the increasing COV, reaching a maximum of 0.114. Therefore, it can be concluded that the SFE and its polar component were sensitive to the changes

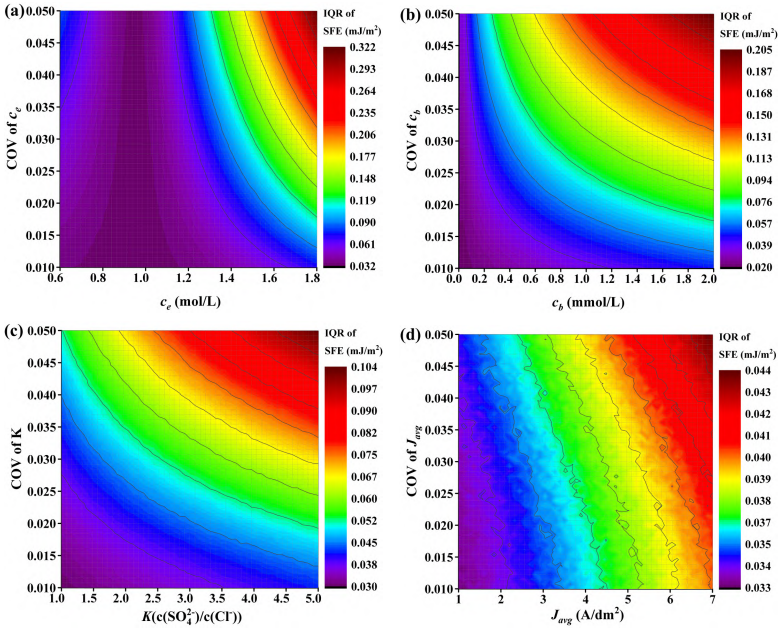

Fig. 6 IQR of SFE at different COVs of the input parameters: (a) c_e; (b) c_b; (c) K; (d) J_{avg}.

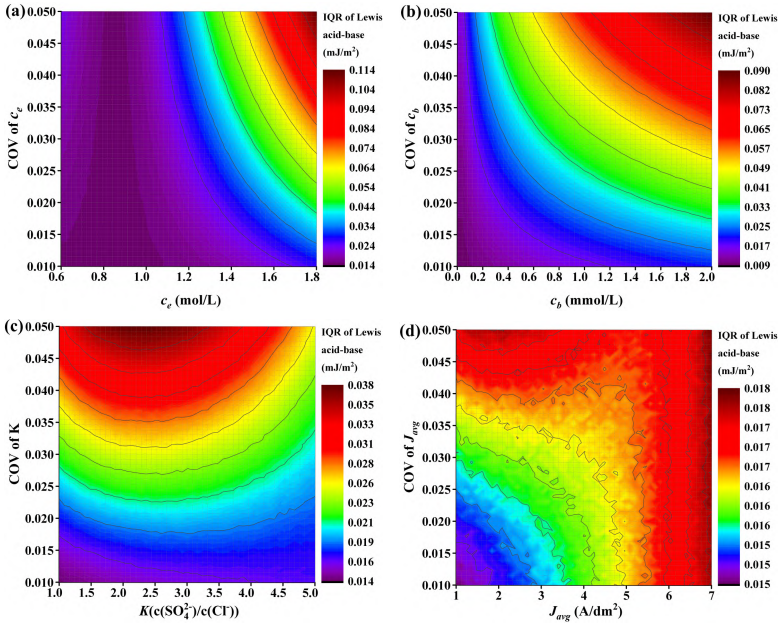

Fig. 7 IQR of the Lewis acid-base component at different COVs of the input parameters: (a) c_e; (b) c_b; (c) K; (d) J_{avg}.

in high-concentration etching solutions. Because the surface morphology tends to become smoother after high-concentration etching (Fig. 2(a,f,g)), resulting in a decrease in SFE. The IQR value of γ_s^{AB} increases with the increase of K and COV, showing a similar trend to γ_s. When K reaches around 2.5, the peak value of IQR reaches 0.038. As shown in Table S3, increasing the sulfate concentration in the deposition solution while reducing the chloride concentration makes the surface smoother and improves the surface energy. When the ratio was greater than 4, the sensitivity of the influence decreased. Similarly, the current density has only a minor effect on the surface polar component of the etched layer.

Fig. S2 shows the XRD patterns of three samples. All the peaks were indexed referring to standard diffraction files, i.e. JCPDS 14–0117 for $Ni(OH)_2$, JCPDS 47–1049 for NiO, and JCPDS 04–0850 for

Ni. Three distinct peaks were observed after etching, corresponding to the Ni (111), Ni (200), and Ni (220) crystal planes. For Sample 1, only the characteristic diffraction peaks of metallic Ni (111), Ni (200), and Ni (220) were observed, indicating the dominant presence of pure nickel. In Sample 4, weak diffraction peaks corresponding to $Ni(OH)_2$ lattice planes appeared alongside the Ni peaks, demonstrating the formation of $Ni(OH)_2$ due to surface hydroxylation. For Sample 5, the intensity of Ni peaks decreased significantly, while assigned $Ni(OH)_2$ lattice planes were clearly detected. Meanwhile, weak peaks of NiO emerged, indicating the further oxidation of $Ni/Ni(OH)_2$ to NiO.

Based on XRD characterization, the diffraction peaks corresponding to NiO and $Ni(OH)_2$ on the rough Ni surface were significantly stronger than those on the smooth Ni surface, verifying that the rough surface is rich in nickel oxide and nickel hydroxide surface phases. Owing to the larger real surface area, higher surface defect density, and more active sites, the rough nickel surface is more readily oxidized to form a thicker and more continuous NiO and $Ni(OH)_2$ layer [36]. From the perspective of surface energy, both NiO and $Ni(OH)_2$ were polar inorganic oxides with abundant surface hydroxyl groups (—OH) [37]. These polar groups greatly increase the polar component of surface energy, resulting in a much higher overall surface energy than that of the non-polar metallic Ni surface. Generally, a higher surface energy corresponds to stronger intrinsic wettability and a stronger affinity toward polar liquids such as water. Meanwhile, the microscale roughness further enhances the actual solid–liquid contact area and introduces a capillary enhancement effect based on the Wenzel model. Therefore, the excellent wettability of the rough nickel surface arises from the synergistic effect of two factors: the high surface energy induced by the polar NiO and $Ni(OH)_2$ layer with abundant hydroxyl groups and the geometric amplification effect of surface roughness on hydrophilicity.

CONCLUSION

A combined electrodeposition-$FeCl_3$ etching process was proposed to prepare hydrophilic nickel coatings on copper substrates. The wettability of the nickel coatings was primarily influenced by the brightener and $FeCl_3$ concentration, followed by anion concentration ratio and current density. The optimal parameters for high hydrophilicity are as follows: $K = 3$, $c_b = 0$, $c_e = 1.2$ mol/l, and $J = 5$ A/dm^2. The surface characterized by a uniformly stacked block structure exhibited the highest hydrophilicity, with a surface roughness of 508 nm and a Lewis acid–base component 14.8% higher than that of the control group. XRD results showed that the rough surfaces were easily oxidized to NiO and $Ni(OH)_2$ (rich in —OH), increasing the polar component of the SFE and intrinsic hydrophilicity, thereby synergizing with roughness to improve wettability per the Wenzel model. This study provides insights into the key determinants of wettability and SFE. These findings provide a reference for designing the surface microstructure of the roller surface to achieve a highly hydrophilic and high surface energy state.

Appendix A. Supplementary data

Supplementary data associated with this article can be found at https://dx.doi.org/10.2306/scienceasia1513-1874.2026.068.

Acknowledgements: This work was financially supported by the Natural Science Foundation of Shandong Province of China [Grant Numbers: ZR2021ME222 and ZR2017MEE036], and Zhangdian District School-City Integration Development Plan Project [Grant Number 2021JSCG0017].

REFERENCES

1. Wu L, Zhou Z, Lan T, Zhang G, Zhang X (2025) Enhancing high-temperature wear resistance of Fe-based amorphous composite coatings via multi-layered TiN_x architecture design. *Surf Coat Tech* **512**, 132449.
2. Bazlov AI, Milkova DA, Zanaeva EN, Ubyivovk EV, Strochko IV, Inoue A (2025) Improvement of the formation ability and soft magnetic properties of Fe-Co-B-Si amorphous alloys with ultrahigh saturation magnetization of 2.0 T by P and C additions. *J Non-Cryst Solids* **666**, 123648.
3. Meenuga S, Kumar Birru A, Kumar Bannaravuri P (2021) Effect of cavitation and spallation on ribbon morphology of $Fe_{73.5}Si_{13.5}B_9Cu_1Nb_3$ alloy in planar flow melt spinning process. *Mater Today P* **47**, 6724–6727.
4. Zhai H, Zhou L, Lv K, Yu S, Li X, Huang Q, Liu T, Chang Y, et al (2025) Numerical simulation of flow and heat transfer behaviors of the melt pool in the melt-spinning process of Nd-Fe-B thin ribbons. *Int J Heat Mass Tran* **241**, 126781.
5. Seino R, Sato Y (2014) Observation of melt puddle behavior in planar flow casting in air. *J Alloy Compd* **586**, S150–S152.
6. Tamura T, Li M (2020) Influencing factors on the amorphous phase formation in Fe-7.7 at% Sm alloys solidified by high-speed melt spinning. *J Alloy Compd* **826**, 154010.
7. Zhang J, Sun F, Liu R, Zhang C, Wang S, Wu G, Mao X (2024) Excellent magnetic properties obtained in planar flow casting Fe-6.5 %Si steel via low strain cold-rolling and annealing. *Mater Design* **244**, 113205.
8. Sowjanya M, Kishen Kumar Reddy T (2017) Obtaining stable puddle and thinner ribbons during planar flow melt spinning process. *Mater Today P* **4**, 890–897.
9. Zhai H, Li X, Yu S, Lv K, Hu Y, Zhu W, Huang Q, Fang Y, et al (2024) Analysis and optimization of the heat transfer behavior in the melt-spinning process of Nd-Fe-B ribbons. *Appl Therm Eng* **248**, 123170.
10. Ahmadian Baghbaderani H, Masood A, Pavlovic Z, Alvarez KL, ÓMathúna C, McCloskey P, Stamenov P (2020) On the mechanisms limiting power loss in amorphous CoFeB-based melt-spun ribbons. *J Magn Magn Mater* **502**, 166535.

11. Naseri M, Myasnikova A, Gholami D, Imantalab O, Mikhailov D, Amra M, Shaburova N, Efimova M, et al (2024) Regulating of wear properties through microstructure engineering in novel cost-effective $Fe_{30}Ni_{25}Cr_{25}Mo_{10}Al_{10}$ high-entropy alloy processed by cyclic closed-die forging. *J Alloys Metal Syst* **7**, 100101.
12. Yue B, Zhu G, Wang Y, Song J, Chang Z, Guo N, Xu M (2022) Research on wettability of nickel coating changes induced in the electrodeposition process. *J Electroanal Chem* **910**, 116146.
13. Xu M, Shen L, Jiang W, Zhao F, Chen Y (2019) Fabrication of Ni-SiC superhydrophilic surface by magnetic field-assisted scanning electrodeposition. *J Alloy Compd* **799**, 224–230.
14. Li B, Zhang X, Ma J, Zhou L, Li H, Liang C, Wang H (2018) Hydrophilicity of bioactive titanium surface with different structure, composition, crystal form and grain size. *Mater Lett* **218**, 177–180.
15. Masood A, Baghbaderani A, Alvarez KL, Blanco JM, Pavlovic Z, Ström V, Stamenov P, Mathuna CO, et al (2021) High-frequency power loss mechanisms in ultra-thin amorphous ribbons. *J Magn Magn Mater* **519**, 167469.
16. Yue B, Chang Z, Wang S, Gao X, Guo N, Wang Y, Zhai X, Zhu G (2023) Wettability study of hydrophilic nickel coatings with high surface energy and high-temperature wear resistance. *Mater Today Commun* **34**, 105470.
17. Ahdour A, Douihi N, Taoufyq A, Aneflous L, Bakiz B, Benlhachemi A (2025) Electrocatalytic and photoelectrocatalytic degradation of Tetracycline using $BaHPO_4$/SSA photoanode: Insights from BBD-RSM and CCD-RSM experimental designs. *Surf Interfaces* **58**, 105874.
18. Do Q, An H, Wang G, Meng G, Wang Y, Liu B, Wang J, Wang F (2019) Effect of cupric sulfate on the microstructure and corrosion behavior of nickel-copper nanostructure coatings synthesized by pulsed electrodeposition technique. *Corros Sci* **147**, 246–259.
19. Cao D, Tang Z, Jiang Y, Liu Z, Guan G, Xu S, Han X (2025) Effect of sodium dodecyl sulfate concentration on the microstructure and mechanical properties of Ni-Co alloy electrodeposited bellows. *Mater Today Commun* **46**, 112582.
20. Suganeswaran K, Nathan SR, Vani R, Mohanraj T (2025) Erosion parameter optimization of AA7075 surface composites with steel slag: A response surface methodology approach for aircraft fuselage applications. *Surf Interfaces* **72**, 107117.
21. Makumbi T, Breustedt B, Raskob W, Ottenburger SS (2025) Parameter uncertainty analysis of the committed equivalent dose coefficients from inhalation of radon progeny in underground uranium mines. *J Environ Radioactiv* **289**, 107751.
22. Dau DT, Nguyen ND, Huynh TN, Pham QH, Nguyen KC, Chu TN, Hoang VK, Phan GTT, et al (2025) Criticality and sensitivity/uncertainty analysis of the DNRR with LEU fuel using MCNP6.3 and the latest data libraries. *Nucl Eng Des* **442**, 114182.
23. Wang X, Gu X, Ding J, Wang Q, Cai Z, Cheng X, Guedes Soares C (2025) Uncertainty analysis of wave loads for multi-connected domain large floating bodies near islands and reefs. *Ocean Eng* **335**, 121676.
24. Peng Q, Zhang Y, He Y, Mao Y (2013) Thermal modeling of chemical vapor deposition on the particle surface subjected to nanosecond laser heating. *Int J Heat Mass Tran* **61**, 675–683.
25. Yue B, Zhu G, Wang Y, Song J, Chang Z, Guo N, Xu M (2021) Uncertainty analysis of factors affecting coating thickness distribution during nickel electrodeposition. *J Electroanal Chem* **891**, 115274.
26. Khan IK, Daud HB, Zainuddin NB, Sokkalingam R, Naheed N, Janisar AA, Inayat A, Rana MS (2025) Standardization of expected value in gap statistic using Gaussian distribution for optimal number of clusters selection in K-means. *Egypt Inform J* **30**, 100701.
27. Han Y, Liu J, Li J, Jiang Z, Ma B, Chu C, Geng Z (2023) Novel risk assessment model of food quality and safety considering physical-chemical and pollutant indexes based on coefficient of variance integrating entropy weight. *Sci Tot Environ* **877**, 162730.
28. Haanappel CP, Voor in't holt AF (2024) Using the interquartile range in infection prevention and control research. *Infec Pre Prac* **6**, 100337.
29. Zhou J, Zhao G, Li J, Chen J, Zhang S, Wang J, Walsh FC, Wang S, et al (2019) Electroplating of non-fluorinated superhydrophobic Ni/WC/WS_2 composite coatings with high abrasive resistance. *Appl Surf Sci* **487**, 1329–1340.
30. Li Y, Liu J, Dong J (2024) Theoretical analysis of contact angle and contact angle hysteresis of Wenzel drops on superhydrophobic surfaces. *Nanomaterials* **14**, 1978.
31. Malm MJ, Narsimhan G, Kokini JL (2019) Effect of contact surface, plasticized and crosslinked zein films are cast on, on the distribution of dispersive and polar surface energy using the Van Oss method of deconvolution. *J Food Eng* **263**, 262–271.
32. Rieke PC (1997) Application of Van Oss-Chaudhury-Good theory of wettability to interpretation of interfacial free energies of heterogeneous nucleation. *J Cryst Growth* **182**, 472–484.
33. Wiącek AE, Jurak M, Gozdecka A, Worzakowska M (2017) Interfacial properties of PET and PET/starch polymers developed by air plasma processing. *Colloid Surface A* **532**, 323–331.
34. Erbil HY (2014) The debate on the dependence of apparent contact angles on drop contact area or three-phase contact line: A review. *Surf Sci Rep* **69**, 325–365.
35. Li K, Xie Y, Liang L, Lin N, Xu L, Chen W, Lu L (2019) Wetting behavior investigation of a complex surface prepared by laser processing combined with carbon films coating. *Surf Coat Tech* **378**, 124989.
36. Chandrakala V, Arputharaj SN (2024) Surfactant assisted wet chemical synthesis of Cu doped NiO@CNF nanocomposites and their photocatalytic behaviour in degrading brilliant green dye under UV light irradiation. *Inorg Chem Commun* **2024**, 112867.
37. Lei Y, Lee Y, Epthing W (2022) Modeling Ni redistribution in the hydrogen electrode of solid oxide cells through $Ni(OH)_2$ diffusion and Ni-YSZ wettability change. *J Power Sources* **545**, 231924.

Appendix A. Supplementary data

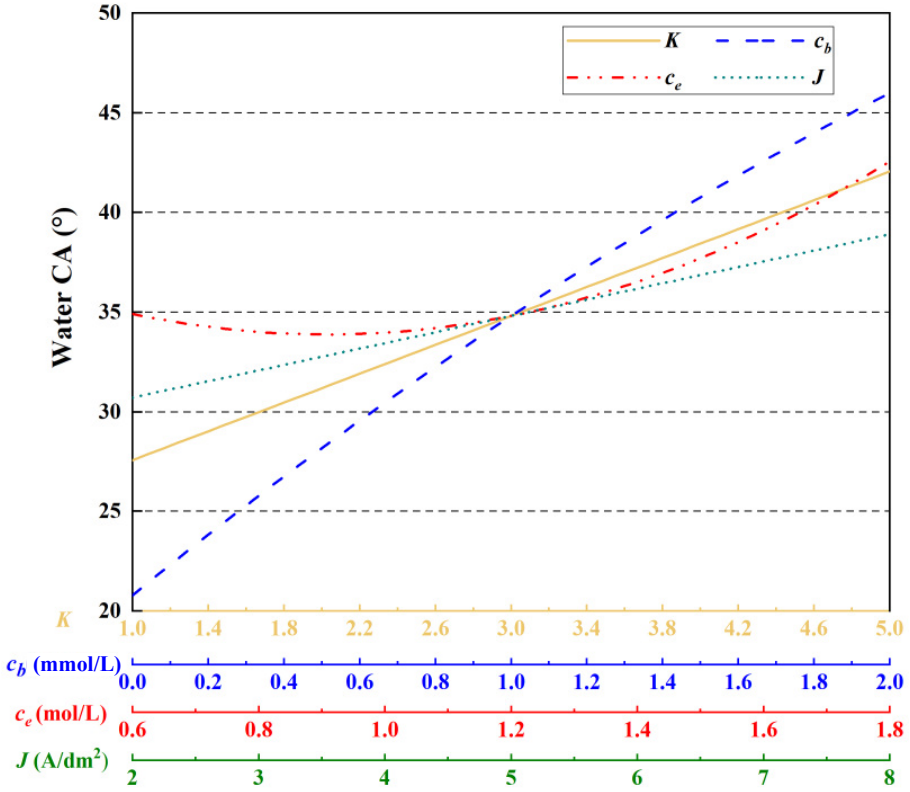

Fig. S1 Trends in water CA with each variable predicted by the RSM model.

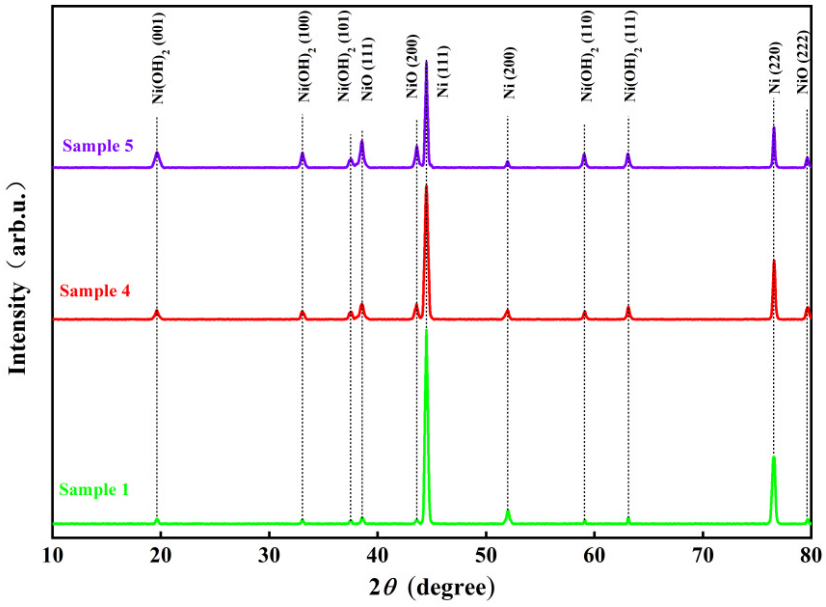

Fig. S2 XRD patterns of different samples.

Table S1 Experimental design of the CCD.

Sample no.	K	c_b (mmol/l)	c_e (mol/l)	J (A/dm^2)	Water CA(°)	Diiodomethane CA(°)	Glycerol CA(°)
1	3	1.0	1.2	5.0	31.3	25.2	28.2
2	1	1.0	1.2	5.0	23.9	23.7	23.0
3	5	1.0	1.2	5.0	37.5	27.4	31.4
4	3	0.0	1.2	5.0	17.9	21.9	19.1
5	3	2.0	1.2	5.0	44.8	29.7	36.6
6	3	1.0	0.6	5.0	33.2	26.1	28.7
7	3	1.0	1.8	5.0	39.0	27.9	32.6
8	3	1.0	1.2	2.0	29.4	25.1	26.7
9	3	1.0	1.2	8.0	33.9	26.3	29.1
10	4	1.5	0.9	6.5	40.2	28.1	33.3
11	3	1.0	1.2	5.0	31.8	25.3	28.0
12	4	0.5	1.5	3.5	29.8	25.2	26.9
13	2	0.5	1.5	6.5	25.4	24.2	23.9
14	2	1.5	0.9	6.5	32.8	25.9	28.3
15	4	1.5	1.5	6.5	44.2	28.9	36.2
16	2	1.5	1.5	3.5	34.6	26.5	29.5
17	3	1.0	1.2	5.0	30.9	25.1	27.8
18	4	1.5	0.9	3.5	39.7	28.1	33.1
19	2	0.5	1.5	3.5	22.6	23.2	22.1
20	4	1.5	1.5	3.5	42.2	28.7	34.9
21	2	0.5	0.9	6.5	21.4	22.9	21.2
22	2	1.5	0.9	3.5	32.4	25.7	28.4
23	4	0.5	0.9	6.5	28.5	24.9	26.1
24	4	0.5	1.5	6.5	32.5	25.6	28.4
25	2	0.5	0.9	3.5	20.4	22.6	20.1
26	4	0.5	0.9	3.5	27.2	24.6	25.2
27	3	1.0	1.2	5.0	31.2	25.3	27.9
28	3	1.0	1.2	5.0	31.6	25.3	28.2
29	2	1.5	1.5	6.5	37.0	27.2	31.2
30	3	1.0	1.2	5.0	31.9	25.5	28.1

Table S2 Average surface roughness of selected samples.

Sample no.	R_a (nm)	R_q (nm)
1	321	410
2	452	572
3	273	368
4	508	634
5	222	307
6	375	486
7	247	333

Table S3 SFE of the selected probe liquids (mJ/m^2).

Probe liquid	γ_l	γ_l^{LW}	γ_l^{AB}	γ_l^+	γ_l^-
Water	72.8	51.0	21.8	25.5	25.5
Glycerol	64.0	15.0	34.0	3.9	57.4
Diiodomethane	50.8	0.0	50.8	0.0	0.0

Table S4 SFE of the selected probe liquids (mJ/m^2).

Sample no.	γ_s	γ_s^{LW}	γ_s^{AB}	γ_s^+	γ_s^-
1	53.04	46.08	6.96	1.38	34.99
2	54.25	46.61	7.64	1.49	39.27
3	51.94	45.26	6.68	1.48	30.14
4	55.20	47.20	7.99	1.52	42.02
5	50.44	44.59	5.85	1.38	24.73
6	52.76	45.75	7.01	1.48	33.31
7	51.57	45.07	6.50	1.45	29.14
8	53.33	46.12	7.21	1.44	36.11
9	52.64	45.68	6.96	1.48	32.79
10	51.38	44.99	6.39	1.45	28.17
11	53.07	46.04	7.03	1.44	34.36
12	53.27	46.08	7.19	1.44	35.82
13	54.00	46.43	7.57	1.49	38.42
14	52.89	45.83	7.06	1.49	33.50
15	50.58	44.67	5.90	1.38	25.20
16	52.52	45.60	6.92	1.48	32.26
17	53.14	46.12	7.02	1.40	35.18
18	51.42	44.99	6.43	1.44	28.64
19	54.50	46.78	7.72	1.49	39.90
20	50.89	44.75	6.14	1.41	26.80
21	54.70	46.88	7.82	1.51	40.43
22	52.90	45.90	7.00	1.44	33.97
23	53.48	46.19	7.29	1.45	36.67
24	52.93	45.94	7.00	1.45	33.86
25	54.94	46.97	7.96	1.56	40.69
26	53.70	46.29	7.40	1.46	37.44
27	53.07	46.04	7.03	1.41	34.93
28	53.02	46.04	6.98	1.40	34.68
29	52.02	45.34	6.69	1.46	30.58
30	53.00	45.97	7.03	1.44	34.32